

# Department of Mathematics and Statistics

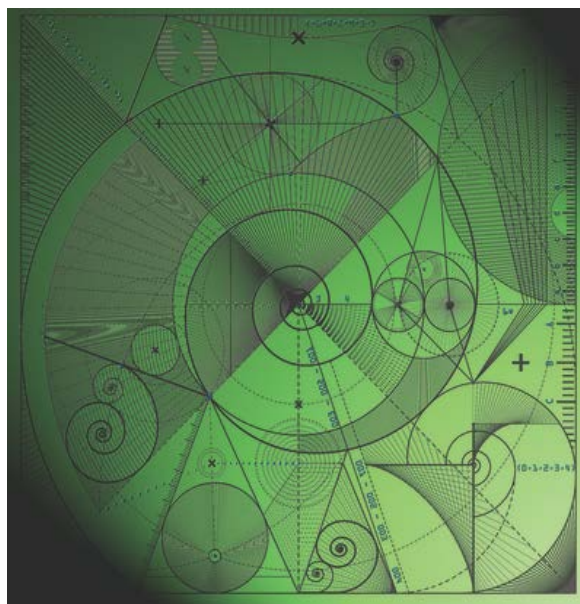
Preprint MPS-2014-06

2 December 2013

## The tube axis and entanglements in polymer melts

by

**Alexei E. Likhtman**



# The tube axis and entanglements in polymer melts

Alexei E. Likhtman

School of Mathematical and Physical Sciences, University of Reading, Reading RG6 6AX, UK

December 2, 2013

## Abstract

Although the tube theory is very popular and successful, the tube concept remains evasive and ill defined. This paper proposes a simple computer algorithm to construct the tube axis as a center line of the cloud of chain configurations at different moments of time. We test this algorithm on trajectories generated from simulations of concatenated well entangled ring polymers, thus avoiding all disentanglement processes. We find that entanglements are clearly manifested through the curvature of tube axis, and we can successfully identify binary and ternary entanglements in molecular dynamics simulations. Several quantitative characteristics of entanglements are reported and discussed.

## 1 Introduction

The tube theory[1] is a standard tool to describe the motion of concentrated polymer solutions and melts. It assumes that if polymers are long enough, their motion is happening predominantly along the contour of the tube (sometimes called a primitive path), and perpendicular motion is somehow restricted by the surrounding chains. This remarkably simple picture has explained many experimental observations and led to several qualitative predictions. It is however notoriously difficult to quantify this idea[2], which explains why the numerous attempts in creating a universal and quantitative theory of polymer dynamics were inconsistent and often unsatisfactory.

In this paper we attempt to quantify the notion of the tube axis by suggesting a computer algorithm which takes the trajectory of one chain from a simulation of some model of entangled dynamics and constructs a tube axis as an average of the chain position during the simulation time. The main difficulty, which we attempt to overcome below, is to define the meaningful average of chain configurations at different moments of time.

In ref.[3] Read et. al. considered a simple network model, where each monomer of a Rouse chain was constrained by an additional harmonic potential representing the influence of other chains. This model is similar to the slip-spring model[4] apart from the fact that slip-links did not slip, i.e. the potentials were always acting on the same monomer. For such simple model Read et.al. demonstrated that the mean path  $\hat{\mathbf{R}}_i$ , constructed from the average positions of each monomer  $i$  over long enough time, had a free energy of a semiflexible chain, with bending modulus directly related to the strength and number of constraining potentials (or slip-springs). However, in reality entanglements are different from network cross-links because the chain can slip through them. This means that the force due to a particular entanglement will be applied to different monomers of the chain, until the chain end passes through the entanglement. After that, the entanglement might disappear all together. This means that averaging monomer positions of the chain sliding through the mesh of entanglements over a time longer than the Rouse time of one entanglement strand  $\tau_e$  would not give meaningful results. Moreover, the results will depend on the averaging time. We illustrate it in the Figure1 below, where we simulated a two-dimensional ring Rouse chain in a square array of point obstacles which can not be crossed. The details of this simulations can be found in ref.[5]. Fig.1 shows 6 configurations of one chain at different moments of time. Since the ring is entangled with the obstacles, the entanglements are permanent and the averaging time can be arbitrarily long. It is obvious that the average positions of all monomers will coincide somewhere in the center of this picture, and thus the mean path will be a point, which is not a very good candidate for the tube axis. The reason for this collapse is that each monomer ( for example monomer  $i = 0$  is shown by slightly larger grey spheres) is traveling around a circle, from one obstacle to another. Thus its average position can not tell us much about individual obstacles.

The solution is clear: instead of averaging positions of monomers with the same index, we need to average positions of the monomers which are in the same section of the tube, or passing the same obstacle. However, there are practical problems in implementing such an idea. One can try for example to construct a principal curve[6],[7],[8], which is a smooth curve defined such that its intersection with the planes perpendicular to itself coincides with the average over points where all chains intersect this plane. This is however problematic for our case of flexible chains, which

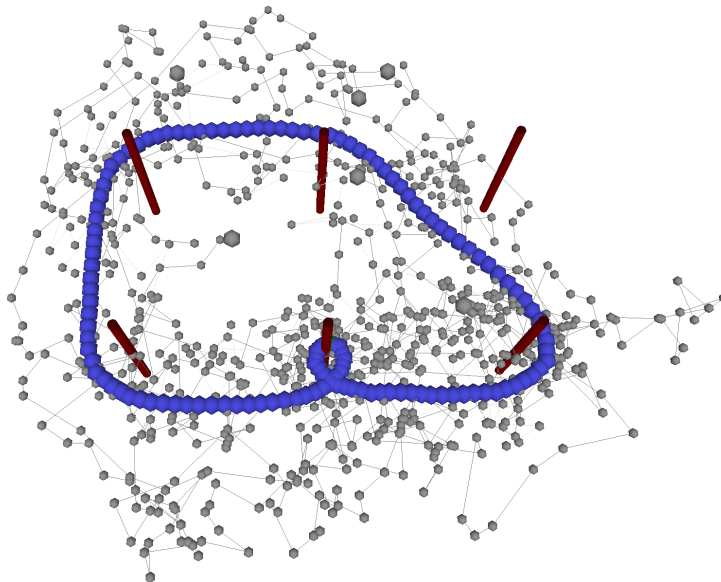


Figure 1: Simulations of 2d Rouse ring chain in an array of obstacles. 6 chain configurations at different moments of time are shown in grey, and the constructed tube axis in blue. Grid spacing is  $g = 4b$ , and the chain length is  $N = 128$ .

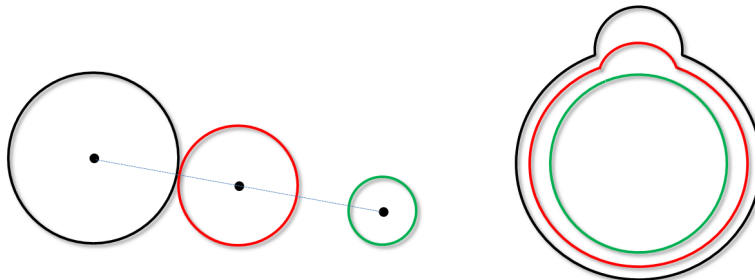


Figure 2: Simplest examples of curve averaging in two dimensions. The average of green and black is shown by red.

intersect each plane many times, and intersections do not necessarily mean that the intersecting monomer is close to the particular obstacle.

In this paper we propose a simple algorithm which averages over many chain configurations and constructs the tube axis, avoiding the problems discussed above. Section 2 outlines the algorithm, whereas section 3 tests the tube axis construction on the simple grid model in 2 and 3 dimensions. Then section 4 provides main results of the paper by constructing tube axis from molecular dynamics (MD) trajectories of concatenated well entangled rings. Section 5 provides conclusions and outlook.

## 2 Tube axis algorithm

First, we seek a meaningful definition of the average between two spacial curves  $\mathbf{r}_1(s)$  and  $\mathbf{r}_2(s)$ , where  $s = 0..1$  is the contour variable. For simplicity, we shall consider closed curves here. What is for example the average in two dimensions of two circles (Fig.2, left) with centres in  $\mathbf{C}_1$  and  $\mathbf{C}_2$  and radii  $q_1$  and  $q_2$ ? To answer this, we first should find for each point  $s$  on the first curve the corresponding point  $s_2(s)$  on the second curve. Once this is done, the average curve can be just composed from the average position of corresponding points

$$\hat{\mathbf{R}}(s) = \frac{\mathbf{r}_1(s) + \mathbf{r}_2(s_2(s))}{2}. \quad (1)$$

For the two circles, it is natural to assume that the corresponding points on the second circle are equidistant if the

points on the first circle are. Thus, if the first circle is given by

$$\begin{aligned}x_1(s_1) &= C_{1x} + q_1 \cos(2\pi s_1) \\y_1(s_1) &= C_{1y} + q_1 \sin(2\pi s_1)\end{aligned}$$

the corresponding points on the second circle will be the ones with  $s_2(s_1) = s_1 + \Delta$

$$\begin{aligned}x_2(s_2(s_1)) &= C_{2x} + q_2 \cos(2\pi(s_1 + \Delta)) \\y_2(s_2(s_1)) &= C_{2y} + q_2 \sin(2\pi(s_1 + \Delta))\end{aligned}$$

where  $\Delta$  is the phase shift between the two configurations. The distance between two curves can be then defined as

$$d^2 = \int_0^1 (\mathbf{r}_1(s_1) - \mathbf{r}_2(s_2(s_1)))^2 ds_1 \quad (2)$$

Using this definition, we postulate that  $s_2(s_1)$  should be chosen to minimize the distance between the two curves. It is easy to show that in two dimensions  $\Delta = 0$  always minimizes this distance, and therefore one can show that the average of two circles is a circle with the centre given by the average of two centres, and with the average radius.

Next, we consider a slightly more complicated case shown in Fig.2 on the right. What shall the average be if the two curves follow each other closely apart from a small part, where the black curve bulges out far from the green curve. This can for example represent an unentangled loop. We expect that such a loop should not strongly affect the averaging in the rest of the chain. Thus, the function  $s_2(s_1)$  should be locally stretched in the area of the bulge, with the aim to obtain the desired result shown schematically by red. To achieve this in the general case, we define  $s_2(s_1)$  as the function which minimizes the functional in eq.2. Then, the average between the two curves is given by eq.1.

It's logical to impose several conditions on the function  $s_2(s_1)$ . For closed curves we must have  $s_2(0) = s_2(1)$ . Besides, we would like to require local monotonicity. To be more specific, we require that  $s_2(s_1) = \text{mod}(f(s_1))$ , where  $f(s_1)$  is a monotonically increasing function and  $\text{mod}(x)$  is the fractional part of  $x$ , i.e.  $\text{mod}(2.3)=0.3$ .

Another required generalization is the definition of the average of many curves. We call

$$\hat{\mathbf{R}}(s) = \frac{1}{M} \sum_{i=1}^M \mathbf{r}_i(s_i(s)) \quad (3)$$

an average of  $M$  curves  $\mathbf{r}_i(s_i)$  if for each curve  $s_i(s)$  minimizes the distance defined in eq.2 from  $i$ -th curve to the average curve.

We now want to define the tube axis as an average of trajectories of one ring over a long time. To apply this definition to the stored trajectories, we must deal with the implicit character of the definition in eq.3. Indeed, the functions  $s_i(s)$  on the right hand side depend in turn on the average path in the left hand side of the equation. This can be treated by the usual iterative method. Another more serious problem is the existence of multiple solutions for  $s_i(s)$ . Besides, the number of unknowns is very large, i.e. if we analyze 1000 stored configurations, and each  $s_i(s)$  is parametrized by 100 numbers, we need to perform minimization over  $10^5$  variables.

The algorithm we propose to deal with the described problems is inspired by the slip-springs model[4], but it is different in details. For the set of saved chain configurations  $\mathbf{r}_k(i)$ , where  $i = 0..N - 1$  is a monomer index (which replaces  $s = i/N$ ) and  $k$  is the time index, we define the tube axis  $\hat{\mathbf{R}}(m)$  with  $m = 0..N/n_0$  by introducing slip-springs connecting each point  $\hat{\mathbf{R}}(m)$  with a monomer  $s_k(m)$  on configurations  $\{\mathbf{r}_k\}$ . Here  $n_0 > 1$  is the average number of monomers between slip-links. We will use  $n_0 = 2$  throughout the paper, but we have verified that  $n_0 = 4$  gives very similar but slightly noisier results. Thus, we define a dynamical system with variables  $\{s_k(m)\}$  and  $\{\hat{\mathbf{R}}(m)\}$  and with the potential energy

$$U(\{s_k(m)\}, \{\hat{\mathbf{R}}(m)\}) = \frac{\kappa}{M} \sum_{k=1}^M \sum_{m=0}^{N/n_0} (\hat{\mathbf{R}}(m) - \mathbf{r}_k(s_k(m)))^2 + \frac{\kappa_{sl}}{M} \sum_{k=1}^M \left( \sum_{m=0}^{N/n_0-1} D^2(s_k(m+1) - s_k(m)) + D^2(s_k(0) - s_k(N/n_0)) \right) \quad (4)$$

where  $\kappa$  is the strength of the slip-springs and  $M$  is the number of stored configurations. The second term here introduces some attraction between the neighboring slip-links with strength  $\kappa_{sl}$ , where  $D(s_1 - s_2)$  means the minimal number of monomers between slip-links sitting on monomers  $s_1$  and  $s_2$ : for linear chains it is equal to  $s_2 - s_1$ , but for rings it follows the minimal image convention similar to the periodic boundary conditions. This attraction is introduced in order to prevent large pieces of the chain to be left without the slip-links and thus ignored by the algorithm. This term imposes a weak constraint on the gradients of the functions  $s_i(s)$ . The dynamic variables are vectors  $\hat{\mathbf{R}}(m)$  and

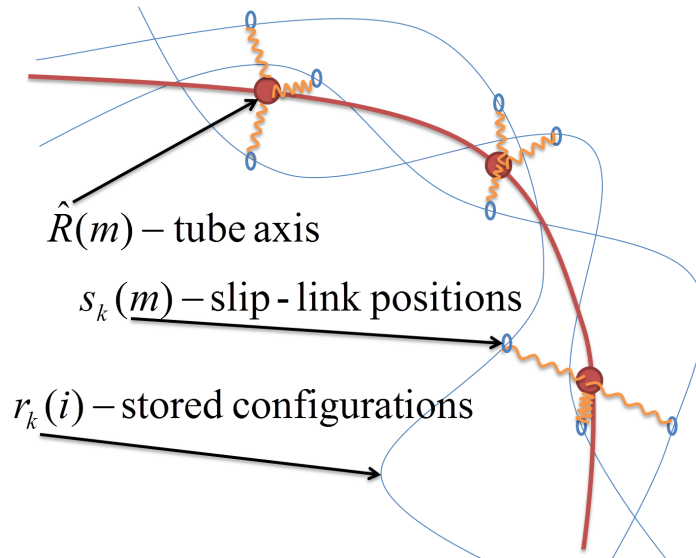


Figure 3: Schematic illustration of the tube axis algorithm. Thin lines show stored chain configurations or mean paths, whereas thick line shows the constructed tube axis.

integers  $s_k(m)$ , and we impose the constraint that slip-links remain ordered on each configuration and can not occupy the same monomer. This constraint is equivalent to monotonicity constraint of  $s_i(s)$  functions. The single occupancy requirement explains why  $n_0$  must be chosen larger than 1: for  $n_0 = 1$  the slip-links would not be able to move because there will be no vacancies for them.

We then run Monte Carlo (MC) simulations, updating  $\hat{\mathbf{R}}(m)$  and  $s_k(m)$  according to the Metropolis algorithm governed by potential energy  $U$  from eq.4. For slip-links positions  $s_k(m)$ , we use two types of moves, one local and one global. The local move is just moving one slip-link to the left or to the right by one monomer. If this monomer is already occupied, the move is rejected. If not, it is accepted according to Metropolis criteria. The global move is a reptation move, when all slip-links on the chain move simultaneously either to the left or to the right. This never creates occupancy clashes, and therefore the acceptance is just given by the Metropolis criteria. Each step we attempt to move each slip-link once on average, attempt 10-100 reptation steps, and perform one  $\hat{\mathbf{R}}(m)$  step for each monomer. During the simulation, we slowly increase the strength of the potential  $\kappa$  to find the optimal  $\hat{\mathbf{R}}(m)$  corresponding to the minimal energy of the system. In practice, the result is independent on details and universal if the rate of change of  $\kappa$  (cooling rate) is sufficiently small.

To improve the efficiency and convergence of the algorithm when analyzing trajectories from molecular dynamics (MD) simulations, instead of instantaneous configurations we use the mean paths, averaged over  $\tau_{av} = 1200$ , which is smaller than  $\tau_e \approx 4000$  for the flexible Kremer-Grest model. Another simplification is that the slip-links are moved according to a standard Metropolis algorithm, but the tube axis variables  $\hat{\mathbf{R}}(m)$  are computed every step as an average of all monomers currently connected to  $\hat{\mathbf{R}}(m)$ . This results in smoother  $\hat{\mathbf{R}}(m)$  path as compared to Metropolis step for  $\hat{\mathbf{R}}(m)$  coordinates, but does not affect the results in any significant way. Before saving results for  $\hat{\mathbf{R}}(m)$ , we average over last 1000 MC steps to provide unique and smooth curve.

### 3 Testing algorithm on toy grid model

#### 3.1 Two-dimensional grid

We first test the algorithm on a simple two-dimensional Rouse model of polymer ring in a grid of point obstacles. We save instantaneous chain configurations with time interval  $\tau_{save} = 10$  in units where temperature, statistical segment and bead friction coefficient are equal to 1. We then use 1000 configurations to construct the tube axis as their average. The results of the algorithm are shown in Fig.1 by the smooth curve made of blue spheres. The constructed curve looks very plausible. Indeed, it shows straight sections between the obstacles, and smooth bends around the obstacles. The tube axis passes at some distance from the obstacles, reflecting an entropic repulsion from them, although their physical size is zero. This repulsion is also apparent in the right upper corner of the figure, where the tube axis is slightly bent downwards because of repulsion from the upper right obstacle, even if the chain is not "entangled" with it in a usual sense. Finally, we notice that the tube axis correctly reflects the chain topology with respect to the bottom obstacle

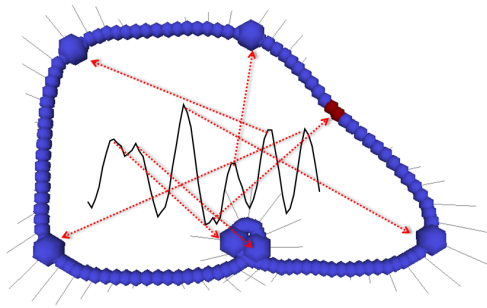


Figure 4: Curvature plot allows associating curvature maximums with individual entanglements.

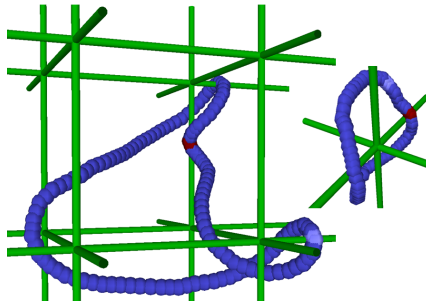


Figure 5: Tube axis for 3d grid model for typical chains,  $g = 4b$ , chain length  $N = 128$  (left) and  $N = 64$  (right).

in the bottom row. This is remarkable since the algorithm does not know about existence of the obstacles: the only input are the chain configurations. Thus, the information about entanglements or obstacles is somehow encoded in the configurations, and our algorithm reveals it. Indeed, we see that we can almost precisely reconstruct the positions of the obstacles by looking at the tube axis only. This can be done by associating the curvature of the tube axis with entanglements. In Fig.4 we plot the curvature of tube axis as a function of monomer index, and point out that the curvature maxima (shown by bigger spheres) correspond to the points where chain is most affected by the obstacles. Indeed it is not surprising: the curvature in the mean path must be induced by an additional force acting on a chain. Thin grey lines show vector curvature — indeed we see that these "forces" are acting on a group of neighboring monomers with a certain direction and the amplitude, which can be described by a Gaussian peak.

### 3.2 Three-dimensional grid model

We now test the algorithm on a 3d grid model described in details in ref.[5]. It is similar to the 2d model used in the previous section, but in three dimensions obstacles are infinitely thin lines forming a simple cubic lattice with the period  $g = 4b$ , where  $b$  is statistical segment of the Rouse chain.

Typical tube axis results together with the grid are shown in Fig.5 for chains  $N = 128$  and  $N = 64$ . We see again that the tube axis nicely follows the grid, with the large curvature corresponding to proximity of the obstacle. For the longer chain on the left we also see that the topology of the tube axis is not identical to the underlying chain topology. Indeed, the strong curvature near the red marker corresponds to the entanglement with the vertical grid line just behind it, but the tube axis does not go behind the grid line. These occasional topology violations are unavoidable since the algorithm does not know about the obstacle positions. Of course for these simple models we can enforce topology preservation, but the aim is to apply the algorithm to the cases where entanglements are not well defined, i.e. to multichain MD simulations. We now turn to this task, which is the main point of this paper.

## 4 Molecular dynamics of concatenated rings

### 4.1 Main results

In order to test our construction on a more realistic model of entangled polymer melt, we use the Kremer-Grest model of purely repulsive Lennard-Jones beads connected by finitely extensible non-linear springs (FENE). The details of the

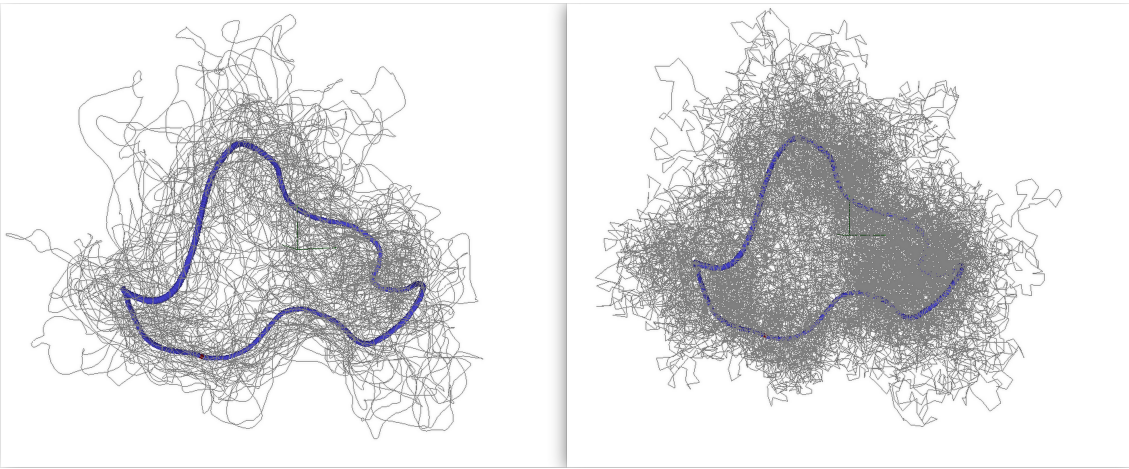


Figure 6: The tube axis of a typical  $N = 512$  ring (blue) shown together with 50 mean path configurations (left) or 50 instantaneous configurations (right) at different moments of time. More configurations were used to construct the tube axis (several thousand)

model are standard and described elsewhere [9]. We do not use any bending or torsional potentials. Following the previous sections, we would like to simulate well-entangled polymer rings. On the one hand, the entanglements will be permanent and we can use very long trajectories to produce accurate averages without worrying about tube destruction by reptation, contour length fluctuations or constraint release. On the other hand, locally we want the structure of our chains and their surroundings to be identical to the structure of entangled linear chains of the same chemistry. This is achieved by first simulating rings with soft potentials, which were adjusted to match the internal monomer distances of the Kremer-Grest model, and which allow chains to pass through each other easily[10],[11]. These rings obey Rouse dynamics on large timescales, and become well concatenated after simulation time of many Rouse times. We then use final configurations of this soft simulation as initial configurations for MD simulation of Kremer-Grest model of rings. We hope that this procedure leads to the same melt structure as the one of linear chains in the limit of long chains  $N \gg N_e$ , where  $N_e$  is an average number of monomers between consecutive entanglements.

We performed MD simulations with  $N_c$  rings each consisting of  $N$  bonds for the total time  $t_{\max}$  in Lennard Jones units, saving instantaneous configurations and mean paths every  $\tau_{av} = 1200$  or  $10^5$  steps (this time is smaller than  $\tau_e \approx 4000$  defined in the tube theory). In this paper we report results from three different systems  $\{N, N_c, t_{\max}\} = \{256, 100, 2.5 \times 10^6\}, \{512, 150, 3 \times 10^6\}, \{1024, 240, 1 \times 10^6\}$ . Each was running on a 12 core node for several months using our own OPENMP code. We then used several thousand stored mean paths to construct the tube axes for all rings independently, using  $n_0 = 2$  and  $\kappa_{sl} = 0.5$ . The virtual spring constant  $\kappa$  is increased during the simulation from  $\kappa = 0.05$  to  $\kappa = 0.4$ , and the typical simulation consists of  $3 \times 10^5$  steps. Increasing it to  $10^6$  steps does not change the results. The number of required steps depends however on the chain length as well as on the trajectory time, so the tests were carried out to make sure that the results do not depend on the choice of the algorithm parameter. All distances in this section will be reported in units of Lennard-Jones  $\sigma$  parameter, which is the monomer diameter. In these units, the bond length is 0.97 and the statistical segment length  $b = \sqrt{\langle R_e^2 \rangle / N} \approx 1.32$ , where  $R_e$  is the end-to-end vector.

Figure 6 shows the result of tube axis construction (blue thick line) for a typical ring of  $N = 512$  bonds. Thin lines show 50 (out of 2500) chain configurations which were used to construct it. The left panel shows the mean paths, which were actually used for the construction, whereas the right panel shows corresponding instantaneous configurations. We see that the smoothness of the paths has increases dramatically from instantaneous configurations to mean paths to tube axis, as expected. We also see that the tube axis lies in the middle of the chains cloud where the chain configurations are relatively straight, but shows prominent features of sudden direction changes and the areas of strong curvature. Interestingly, the spread of the mean paths around the tube axis is almost the same as the spread of instantaneous configurations. This means that many fluctuations are not averaged out by calculating the mean paths, and averaging over much longer times, performed by our algorithm, is essential to obtain unique tube axis. The spread is further analyzed quantitatively in Fig.8.

The reasons for these sudden curvature peaks are interactions with other chains, as revealed by Fig.7. Here we performed tube axis constructions for all 150 rings in the box independently of each other, and show in the left panel the tube axis for one ring together with pieces of tube axes of all other rings which happen to pass our chosen tube

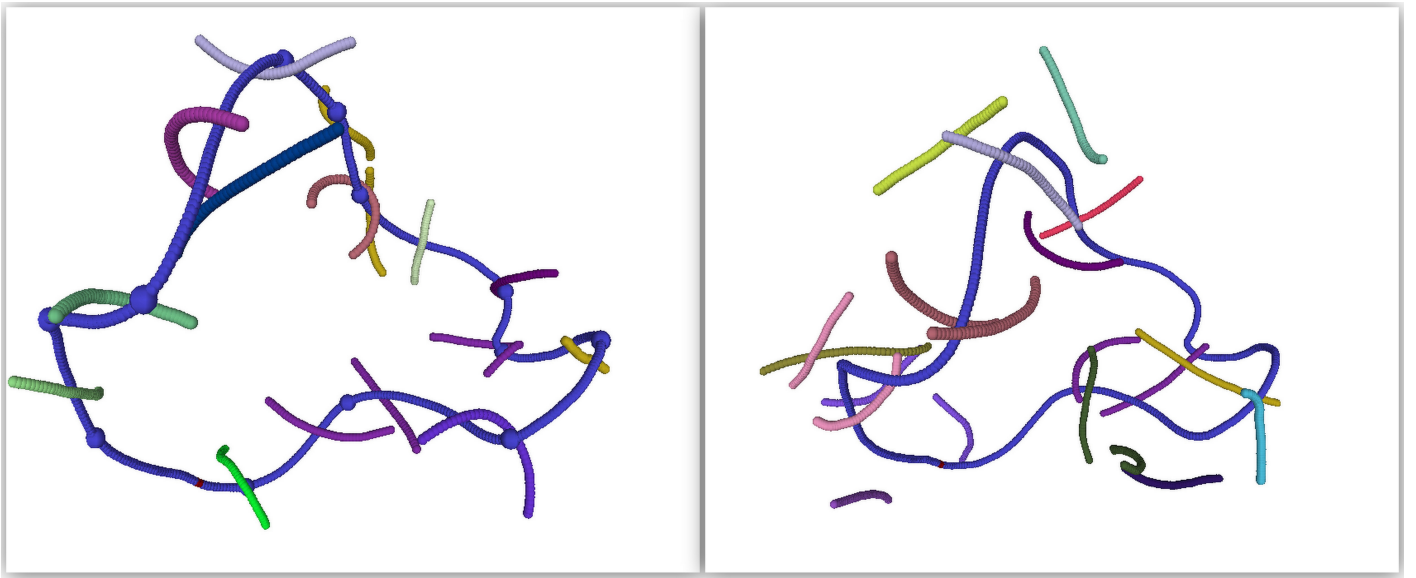


Figure 7: Tube axis for the same chain as in Fig.6 together with pieces of tube axis of other chains, which passed the blue tube axis within less than  $r_c = 1.5$  (left) and other pieces with minimum distance between 1.5 and 3 (right).

axis within a critical distance  $r_c = 1.5$  (in units of Lennard-Jones  $\sigma$ ). We see very clearly that all turns of the tube axis are caused by a close contact with the axes of another chain. In contrast, the more distant contacts, shown in the right panel of Fig.7, do not seem to be correlated with the chain curvature. Of course the cut-off at  $r_c = 1.5$  is not sharp, and there are occasional entanglements with larger  $r_c$ . The particular value 1.5 is just a reasonable estimate, with additional support provided by Fig.13 later.

This intuitive picture is quantified by plotting the absolute value of the curvature of the tube axis, defined as

$$c(i) = \frac{\mathbf{R}_{i+\Delta} + \mathbf{R}_{i-\Delta} - 2\mathbf{R}_i}{\Delta^2}$$

The choice of  $\Delta$  is guided by two criteria: it should be larger than 1 to avoid the influence of small scale fluctuations, but smaller than the typical distance to the next entanglement. Following these two limitations, we set  $\Delta = 10$  monomers.

Fig.8 shows that the curvature of the tube axis exhibits very distinct maxima, and each of such maxima corresponds to a close contact with another chain (the pieces of tube axes which pass a selected tube axis within  $r_c = 1.5$  are shown by different colours). We mark curvature maxima on the blue tube axis with larger blue spheres, and the monomers in contact with other chains by yellow spheres. We see that many yellow spheres are close to the blue spheres. The particular chain presented here has also two self-entanglements marked by orange arrows, thus 5 curvature maxima do not correspond to contacts with other chains. Such curvature plot clearly leads to two important conclusions. First, the selected chain feels discrete number of constraint forces rather than a continuous field. This picture is referred to as entanglements concept, whereas the continuous field is a key premise of the tube theory. The second conclusion is that the information about all contacts is encoded in the tube axis in a very compact form, and one can infer the reasons for a particular tube axis conformation. We have also defined the tube radius as the square root of the average squared length of all springs attached to point  $R_i$  of the tube axis. This is shown in Fig.8 by the dashed and dotted lines, corresponding to the average distance to mean paths and to instantaneous configurations. In contrast to the curvature plot, the tube radius does not seem to show any prominent features at entanglement points and is remarkably close to constant. It is also smaller than the tube radius reported by Zhou and Larson[8], although they used a different definition. We also confirm the conclusion drawn initially from Fig.6: the average distance from the tube axis to the mean paths (about 2.3) is quite similar to the distance to the instantaneous configurations (about 2.5).

We find it quite remarkable that the entanglements can be seen very clearly by naked eye just by plotting the tube axes of a selected rings and its neighbors. This is further illustrated in Fig.9 with 4 different rings and all rings those tube axis have passed within  $r_c = 1.5$  of the selected blue ring. One can clearly see that the particular tube axis shape is created by the other chains entangled with it.

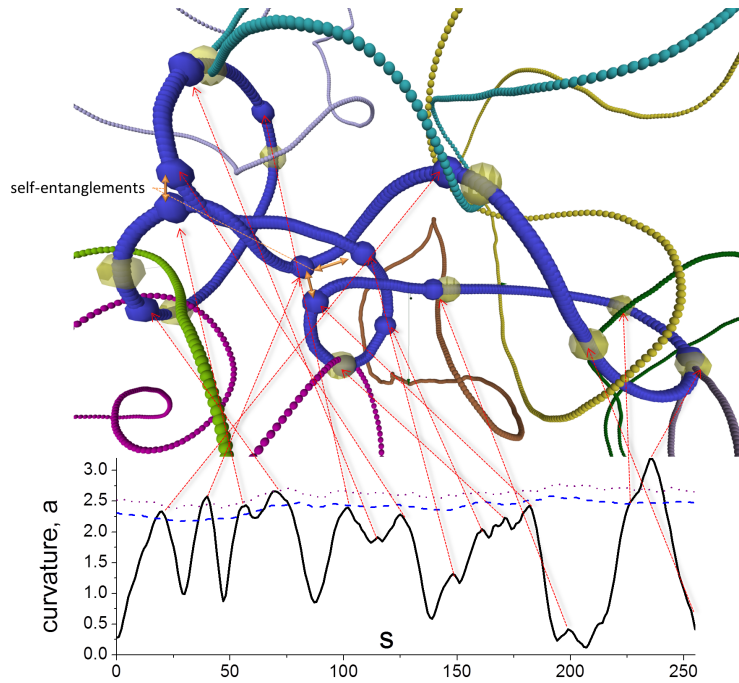


Figure 8: Tube axis of one  $N = 512$  chain (blue) together with all other axes which pass within a cut-off distance  $r_c = 1.5$ . The plot at the bottom shows the curvature of the tube axis along the chain (solid line, scaled arbitrary), and the arrows show the points on the tube axis corresponding to the curvature maxima. The dashed line shows the tube radius in units of  $\sigma$  computed with mean paths, whereas dotted line shows the same using instantaneous chain configurations.

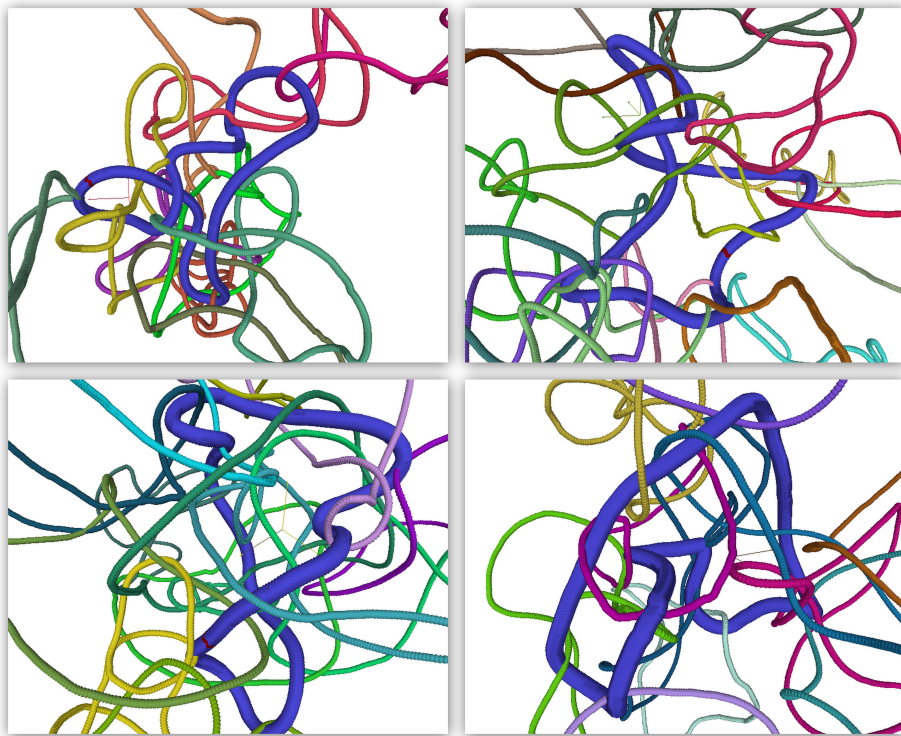


Figure 9: Tube axis for 4 different rings from  $N = 512$  simulation (thick blue), together with tube axis of all other rings which passed within  $r_c = 1.5$  of the selector ring.

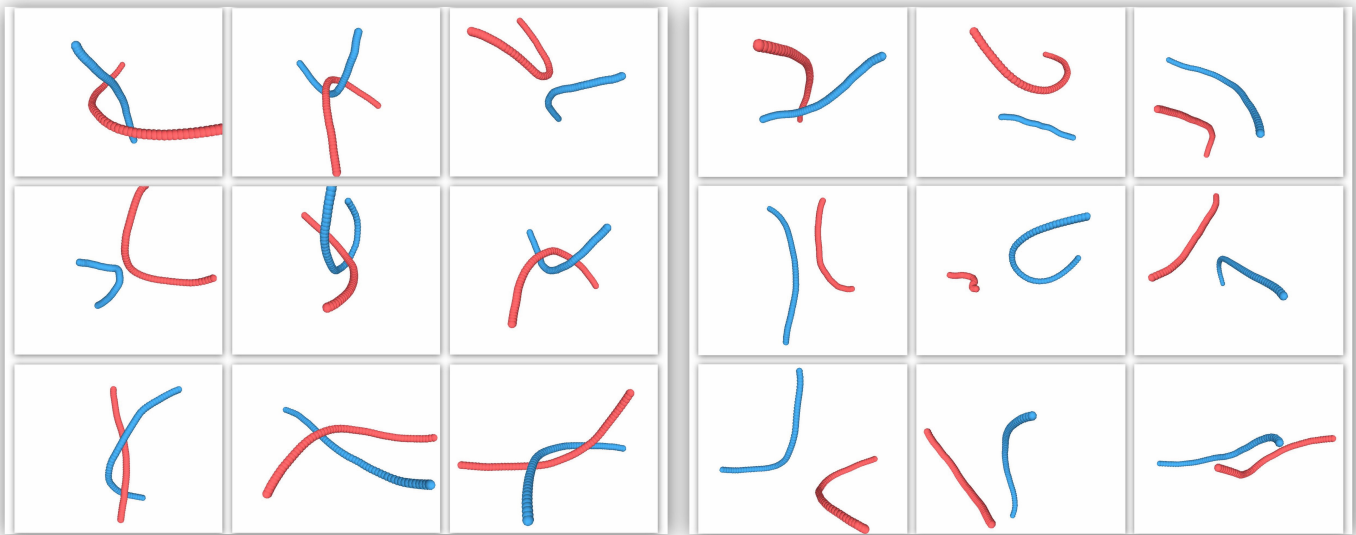


Figure 10: Randomly selected contacts with  $r_c < 1.5$  (left) and  $1.5 < r_c < 3$  (right).

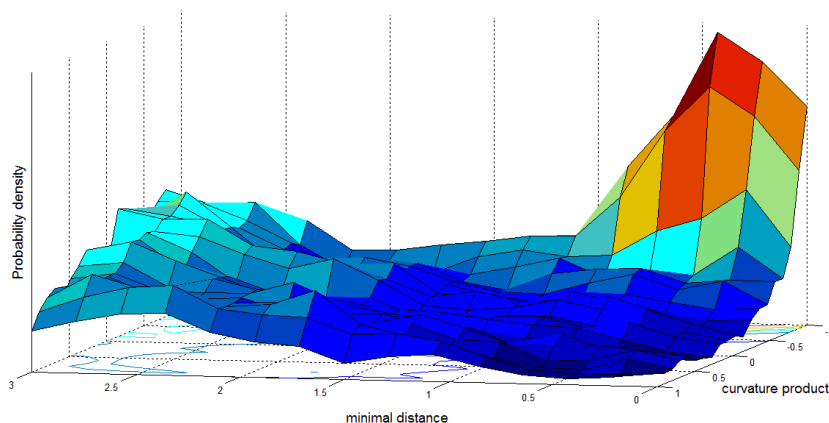


Figure 11: Probability density to observe a close contact between two tube axis as a function of minimal distance between them and their curvature product.

## 4.2 Individual entanglements

We now turn our attention to individual entanglements, which we define as close contacts between the tube axes of different chains. We find that contacts with minimal distance between two tube axes  $r_c < 1.5$ , shown in Fig.10, left panel, indeed look like simple entanglements. In contrast, contacts with larger minimal distances  $1.5 < r_c < 3$  do not seem to be correlated with each other.

To quantify this, we notice that vector curvature of two chains participating in a simple entanglement should be anti-parallel with respect to each other. We define curvature product for each entanglement as

$$c_p = \frac{\mathbf{c}_{j_1}(i_1) \cdot \mathbf{c}_{j_2}(i_2)}{|\mathbf{c}_{j_1}(i_1)| |\mathbf{c}_{j_2}(i_2)|}$$

where  $j_1$  and  $j_2$  are chains participating in the entanglement and  $i_1$  and  $i_2$  are their monomers which are closest to each other. Clearly,  $c_p$  is just the cosine of an angle between two curvatures, with  $c_p \approx -1$  corresponding to the anti-parallel orientation. Fig.11 shows the probability density to observe an entanglement with a particular minimal distance and curvature product in the melt of  $N = 512$  rings. We see that for the contacts with small minimal distance (tight contacts) there is a high probability to find a negative curvature product, whereas for less tight contacts the curvature product distribution is roughly uniform.

Next we can ask the question whether entanglements on one ring interact with each other. This can be tested by calculating the pair correlation function  $g(s)$ , which is proportional to the probability to find another entanglement  $s$

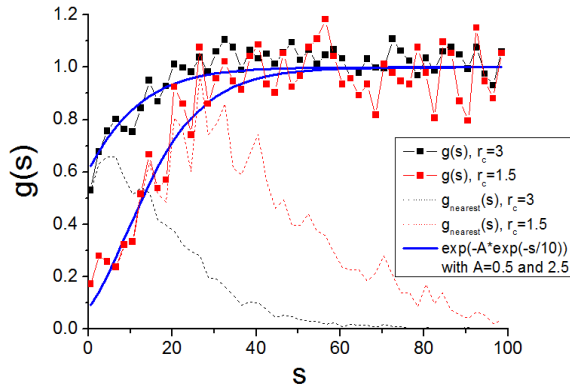


Figure 12: Pair correlation function for two different cut-off radii as a function of distance along the chain: for all entanglements (squares) and for nearest on the chain (dashed lines).

monomers away from any given entanglement along the chain. If we define entanglement positions on the chain by the monomer closest to another chain, the resulting pair correlation function is given in Fig.12 by the red squares. The function is normalized by the average entanglement density such that  $g(s \rightarrow \infty) = 1$ . Clearly, such  $g(s)$  corresponds to the short-range effective repulsion between entanglements along the chain. The effective potential  $U_{ent}(s)$  is approximately  $-k_B T \ln(g(s))$  and can be fitted by an exponential form  $A \exp(-s/s_0)$ , with  $A = 2.5$  being the strength of the potential. The parameter  $s_0$  has the physical meaning as the range of the repulsion potential between the entanglements, and it is interesting to see that our result  $s_0 \approx 10$  is smaller than the typical distance between entanglements ( $N_e \approx 30 - 50$  from Fig.13). This repulsion is caused by the excluded volume interaction between the chains forming neighbouring entanglements. If much more contacts are included with the cut-off distance increased from  $r_c = 1.5$  to  $r_c = 3$ , we find that the interaction potential have similar range but smaller amplitude (black squares). For completeness, we also report similar pair correlation function for the neighboring entanglements only, which is proportional to the probability distribution of number of monomers between neighboring entanglements on the chain (dashed lines in Fig.12). They follow  $g(s)$  for small  $s$  and decay exponentially for larger  $s$ , similar to the ideal gas statistics. Tzoumanekas and Theodorou [12] reported this function for the distance between consecutive kinks in the primitive path of the chain, which they fitted by the difference of two exponentials. We found that our results do not follow this functional form, and that  $g(s)$  function is more informative in deducing an effective repulsion between entanglements, which can be used in the slip-spring model.

We would like to stress that the purpose of this paper is to understand what entanglements and tube axes are, rather than to count them. This is because we do not believe that counting entanglements is meaningful without having a reliable model which can use this number to predict all dynamical properties. Tube model clearly fails to do so for variety of reasons described elsewhere[11],[5]. The slip-spring model on the other hand does a good job[13], but requires strength of entanglements as well as their number. We therefore leave the slip-spring parameters estimation to our future work. For completeness however, we compute here the number of contacts between different rings, which is clearly a function of the cut-off distance in the definition of what do we mean by the close contact. This is shown in Fig.13 for three different systems simulated as  $N_e = N / \langle Z \rangle$ , where  $Z$  is the total contact number of each tube axis. Horizontal lines show  $N_e$  estimate from the number of curvature maxima, as shown in Fig.8. This definition probably misses few contacts, which produce shoulders rather than the separate maxima. It is interesting that these two estimates intersect at the cutoff distance around  $r_c = 1.5$ , which agrees with our previous conclusion that  $r_c \approx 1.5$  is a reasonable cut-off value. Note however that our estimate  $N_e \approx 35 - 40$  is smaller than the tube theory estimates  $N_e \approx 70 - 90$  obtained by the primitive path analysis (PPA) [14],[15]. This is probably due to the inconsistency of the tube theory equations used in PPA analysis.

We have also measured the length of the tube axes  $\langle L \rangle$  and its average fluctuations  $\Delta L^2 \equiv \langle (L - \langle L \rangle)^2 \rangle$ . Following the tube theory definitions outlined again in our recent paper[5], the tube Kuhn step  $a$  (often called tube diameter) and the statistical segment of the effective Rouse chain inside the tube  $b_{1d}$  are defined as

$$a = \frac{\langle R_e^2 \rangle}{L}; \quad b_{1d}^2 = \frac{3\Delta L^2}{N} \quad (5)$$

The computed tube theory parameters (in units of Lennard-Jones  $\sigma$ ) are

$$a = 11.5 \pm 0.5; \quad b_{1d}^2 = 1.25 \pm 0.1,$$

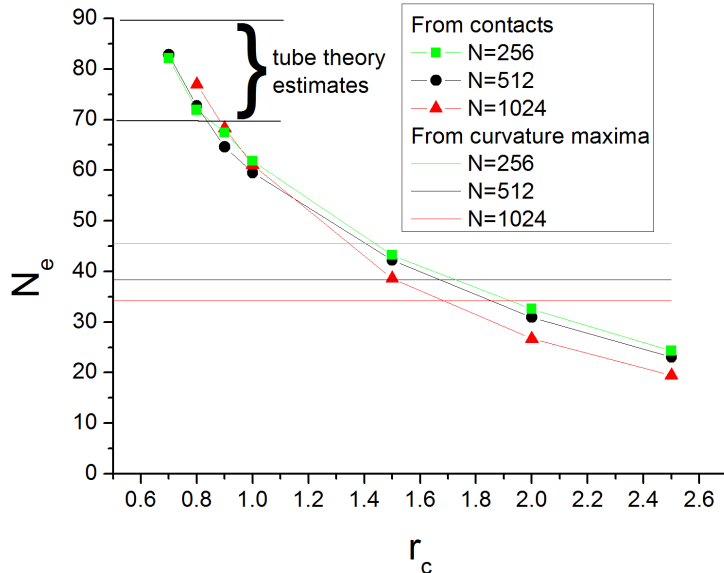


Figure 13: Average number of monomers between close contacts and between curvature maxima.

For comparison, the usual 3d statistical segment length for our chains is  $b_{3d}^2 \approx 1.75$ , and the tube theory usually assumes that  $b_{1d} = b_{3d}$ . One should also note that the tube radius measured by our tube axis algorithm (Fig.8, dotted line) is around 2.5, and therefore is significantly smaller than the tube Kuhn step length.

### 4.3 Triple entanglements

The pictures discussed so far provide clear evidence that many entanglements are binary, i.e. involve a close contact and strong interaction between two chains. This results in anti-parallel curvature of their tube axes in the vicinity of entanglements. However, it is clear that there are many aspects in which entanglements are multi-chain events. For example, deleting one entanglement can cause other entanglements to disappear and appear, several entanglements among the same chains are strongly correlated etc. In this paper we consider the simplest multi-chain effect, which is a possibility of triple entanglement. We say that a pair of binary entanglements on chain A with chains B and C participate in a triple entanglement if chains B and C are also entangled with each other. Besides that, we require that the number of monomers between entanglements along chains A, B and C should be less than a cut-off distance  $s_c$ .

Fig.14 shows 9 randomly selected triple entanglements from our system with the cut-off  $s_c = 50$ . It is quite clear that in these cases interactions are not binary. Then we can measure the fraction  $\phi_{trip}$  of pairs of entanglements on the same chain within monomer separation  $s_c$  which participate in a triple entanglement. We find that  $\phi_{trip} = 0.2 \pm 0.02$  for  $N = 256, 512$  and  $1024$  if we use  $r_c = 1.5$  and  $s_c = 50$ . Changing monomer cut-off to  $s_c = 100$  results in a very slight decrease to  $\phi_{trip} = 0.18 \pm 0.02$ . Reducing minimal distance cut-off to  $r_c = 1$  results in a significant decrease of the triple entanglement fraction to  $\phi_{trip} = 0.11 \pm 0.05$ , but we do not think this is very reasonable estimate because many triple events go missing with  $r_c = 1$ . If we increase the cut-off to  $r_c = 2$ , the fraction of triple entanglements increases to  $\phi_{trip} = 0.29 \pm 0.02$  for  $s_c = 50$  and to  $\phi_{trip} = 0.25 \pm 0.03$  for  $s_c = 100$ . Thus, we conclude that the fraction of triple entanglements is significant, somewhere in the range of 20 – 30%, and might affect the dynamics in at least two possible ways. Triple entanglements must be stronger in average in a sense that they restrict the chain more than a binary entanglement, but also might be more difficult to disentangle. Secondly, the constraint release in triple entanglements will be different. For example, if the red chain in the central entanglement of Fig.14 will reptate away, both other chains will be disentangled as well. This is of course not true for many other examples in the same figure. We leave the study of constraint release to further publication.

Although triple entanglements do exist in significant number, their fraction is still relatively small. This means that binary entanglements still dominate the behavior of entangled melts, and that the role of even more complex entanglements involving more than 3 chains is even smaller.

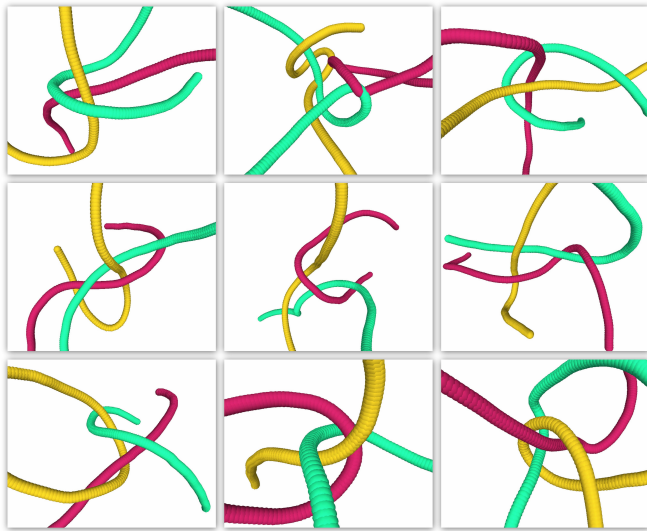


Figure 14: Randomly chosen examples of triple entanglements.

#### 4.4 Iso-configurational averages and primitive path analysis

The main drawback of the proposed tube axis construction is that it requires long trajectories of the length of order  $100\tau_e$  to produce unique and well defined results ( $\tau_e \approx 4000$  in Kremer-Grest model). This is problematic for the usual linear or branched polymers, which will renew part or even all of their entanglements during this averaging period. Fixing chain ends to stop tube renewal is not a good idea either: we find that these fixed points reduce fluctuations available to the network of entanglements significantly, and provide many "false positives" in entanglement detection algorithms. In order to get an instantaneous snapshot of entanglement structure, one has to use shorter averaging times of order of  $\tau_e$ , or use topological constructs like the primitive path analysis (PPA).

The primitive path analysis [14],[15] however has several drawbacks comparing to the present method. First, the primitive path construction is based on the assumption that the shortest path is the one which the chains will choose to diffuse along. This is of course a simplification, confusing the average with the minimum. In contrast, the tube axis construction is based on the actual polymer configurations. Second, the primitive path construction is not unique, and starting from different parts of the rings trajectory will lead to different results. Thus, only the average total primitive path length is reproducible. This is in contrast to uniqueness of tube axis illustrated below. Third, the analysis of the PPA results contains very crude assumptions about their statistical properties, leading to significant underestimation of the number of entanglements, as illustrated in Fig.13.

Reducing averaging time results in less smooth paths, with much more small curvature maxima due to random fluctuations and not due to interactions with other chains. A tempting way to kill these fluctuations is iso-configurational ensemble averaging[16], which is widely used in glass community[17]. Instead of averaging over a long trajectory, it relies on many short trajectories started from the same configurations. If the length of such trajectories is of the order of  $\tau_e$ , then slip is not important and one can just average monomer positions over the final configurations, or over the mean paths collected during these runs. The hope is then that all random fluctuations will be averaged out and the unique tube axis will emerge, which would not depend on time if all entanglements are permanent. We test this idea below by running 100 trajectories of length  $\tau_{iso} = 1.2 \times 10^4$  in units of Lennard-Jones times (this is slightly longer than  $\tau_e$ ). We then average the positions of every monomer over the run time and over 100 trajectories. To test the uniqueness of the obtained tube axis, this was done starting from two different initial configurations, which were frames of the same run  $1.2 \times 10^6$  time units away from each other. These two iso-configurational averages are shown in Fig.15 in red. One can see that these curves also show pronounced curvature maxima, but some of them are only present in one of the curves, meaning that they were not caused by entanglements (which are permanent), but by the long-lived fluctuations. These are compared with 2 tube axes (green), constructed using the first part of the trajectory (time  $1.2 \times 10^6$ ) and the second one. It is apparent that our tube axes are closer to each other than the iso-configurational averages. Besides, the distance between them decreases with increasing trajectory length, whereas iso-configurational averages do not change any more if more trajectories are used for the averages. In our opinion, this shows that some fluctuations in the entanglement network live significantly longer than  $\tau_e$  and therefore can not be averaged out by iso-configurational average. Increasing trajectory length will introduce problems discussed in the beginning of this paper, which can only be avoided by our method.

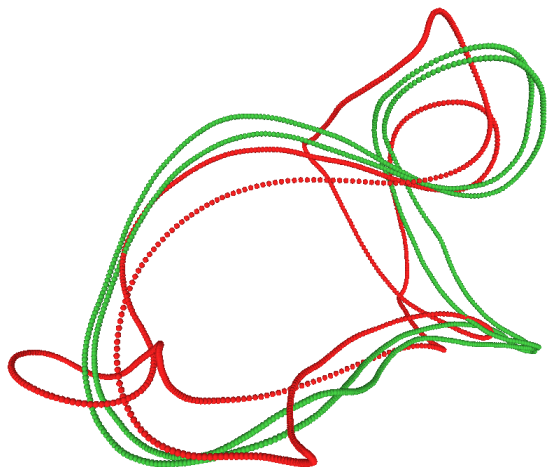


Figure 15: Tube axis construction using first 1000 and second 1000 mean paths (green) compared to two iso-configurational ensemble average paths (red).

## 5 Conclusions

In summary, we have proposed a simple computer algorithm to construct the tube axis as an average path which a chain follows in entangled polymer melts and solutions. The algorithm averages over thousands of stored chain configurations and finds a smooth path in space which minimizes the distance to all configurations. The procedure seem to be robust and converges to a unique solution as the number of used trajectories increases.

Crucially, constructed tube axis have very distinct features, revealed for example as maxima of curvature along the axis. We have demonstrated that these maxima are strongly correlated with close contacts with tube axes of other chains, which is to be expected. Indeed, a free chain with fixed ends would have a straight line as its tube axis, and therefore the curvature must be caused by the interactions with other chains. What is surprising is the discreteness and predominantly pairwise nature of these interactions. This is in contrast to the popular interpretation of the packing length scaling, predicting that about 20 chains are needed in a volume of tube diameter to create an entanglement. Our results show that this does not mean that each entanglement is created by 20 chains. Instead, it should be reinterpreted in probabilistic terms: if there are 20 chains in a volume  $a^3$ , on average one entanglement will be formed between two chains in this box. Triple entanglements also exist, but their role is smaller. An additional output of the tube axis construction is the value of the tube radius, defined as an average distance from the tube axis. It is found to be around  $2.5\sigma$ , which is significantly smaller than the tube theory estimate. This discrepancy highlights that one should not assume that the tube diameter is equal to the tube Kuhn segment length.

The results of this paper do not provide a recipe for modelling entangled melts. For example, knowing the tube axis does not yet mean that one can make predictions about dynamics, or even about the plateau modulus. These aims will be addressed in the next publication. Instead, this paper is designed to illustrate the interplay between the tube and entanglement concepts and provide some visual evidence of entanglements and a way of quantifying their strength through the curvature of the tube axis.

**Acknowledgement.** I thank Tim Palmer, M.Ponmurugan, Jing Cao and Daniel Read for constructive discussions and collaboration prior to this work. I also thank Scott Milner for drawing my attention to ring polymers. This work was supported by Engineering and Physical Sciences Research Council (EPSRC), UK, grant H5094900.

## References

- [1] M. Doi, S. F. Edwards, *The theory of polymer dynamics* (Clarendon Press, New York, USA, 1986).
- [2] S. F. Edwards, *Proc. Phys. Soc.* **92**, 9 (1967).
- [3] D. J. Read, K. Jagannathan, A. E. Likhtman, *Macromolecules* **41**, 6843 (2008).
- [4] A. E. Likhtman, *Macromolecules* **38**, 6128 (2005).
- [5] A. E. Likhtman, M. S. Talib, B. Vorselaars, J. Ramirez, *Macromolecules* **46**, 1187 (2013).

- [6] T. Hastie, W. Stuetzle, *J. Am. Stat. Assoc.* **84**, 502 (1989).
- [7] E. Vanden-Eijnden, M. Venturoli, *The Journal of chemical physics* **130**, 194103 (2009).
- [8] Q. Zhou, R. G. Larson, *Macromolecules* **39**, 6737 (2006).
- [9] A. E. Likhtman, S. K. Sukumaran, J. Ramirez, *Macromolecules* **40**, 6748 (2007).
- [10] J. Cao, A. E. Likhtman, *Phys. Rev. Lett.* **104** (2010).
- [11] A. E. Likhtman, *Polymer Science: A Comprehensive Reference* (Elsevier B.V., 2012), vol. 1, pp. 133–179.
- [12] C. Tzoumanekas, D. N. Theodorou, *Macromolecules* **39**, 4592 (2006).
- [13] S. K. Sukumaran, A. Likhtman, *Macromolecules* **42**, 4300 (2009).
- [14] R. Everaers, *et al.*, *Science* **303**, 823 (2004).
- [15] R. S. Hoy, K. Foteinopoulou, M. Kroger, *Phys. Rev. E* **80**, 031803 (2009).
- [16] W. Bisbee, J. Qin, S. T. Milner, *Macromolecules* **44**, 8972 (2011).
- [17] A. Widmer-Cooper, P. Harrowell, H. Fynewever, *Physical Review Letters* **93**, 135701 (2004).